Sánchez-Sesma *et al.*
Earth, Planets and Space (2023) 75:29
https://doi.org/10.1186/s40623-023-01780-0

Earth, Planets and Space

FULL PAPER

Open Access

A new closed analytical solution for the elastodynamic half-space Green's function

Francisco J. Sánchez-Sesma[1*], Francisco Luzón[2], Antonio García-Jerez[2], Mathieu Perton[1], Mario A. Sáenz-Castillo[3] and César A. Sierra-Álvarez[3]

Abstract

The elastodynamic half-space Green's function has been the subject of research for more than a century since the Lamb's classical solution. Here, we revisit the problem and present a new closed analytical solution, in frequency domain, based upon the Principle of Equipartition (EQP) of Energy. This principle asserts that the imaginary parts of the Green's tensor components equal the average cross-correlations of the fields generated by the uniform incidence of *P* and *S* body waves and by Rayleigh surface waves with amplitudes weighted by partition factors. The real part of the Green's function is the Hilbert transform of the imaginary part. We validate our results by comparing synthetic seismograms of well-known solutions for surface and buried forces and discuss the implications of this new solution. Constructing synthetic diffuse fields is a first step for identifying them in nature.

Keywords Elastic half-space, Elastodynamic Green's function, Equipartition, Cross-correlations, Synthetic diffuse fields

Graphical Abstract

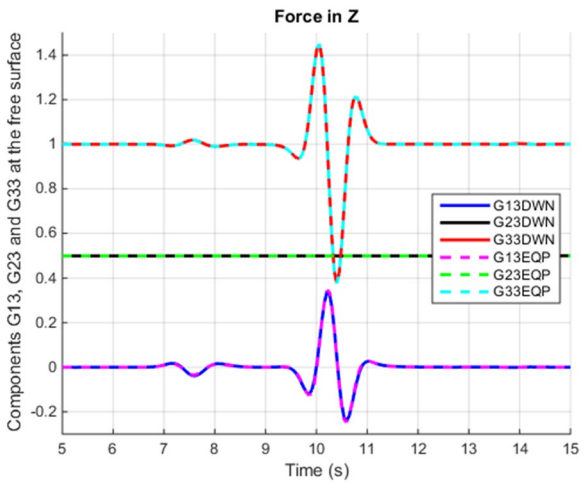

*Correspondence:
Francisco J. Sánchez-Sesma
Sesma@Unam.Mx
Full list of author information is available at the end of the article

Introduction

The impulsive normal load at the surface of an elastic half-space was studied in a classical work by Lamb (1904). This solution is based on integral representations and the explicit passage to the time domain became premonitory of methods developed some decades later. An excellent account of Lamb's problem can be found in Kausel (2013) who pointed out that the first truly complete solutions to Lamb's problem were obtained by Pekeris (1955) and Chao (1960). Significant improvements are due to Johnson (1974), Mooney (1974) and Richards (1979). Moreover, sundry numerical computations of the Green's function associated to Lamb's problem, are due to Johnson (1974). Explicit formulae have been recently given for the displacement at the surface of an elastic half-space for a buried point force in what can be called the 3D Lamb's problem (see Liu et al. 2016; Feng and Zhang 2018). Even if their results are given in terms of elementary algebraic expressions and elliptic integrals as well, the complexity of computation is considerable.

The calculations of Green's function in the frequency domain start with the integral representation in cylindrical coordinates in terms of integrals along the radial wavenumber. Practical solutions like the asymptotic behavior of Rayleigh waves could be obtained from the residues at the Rayleigh simple pole in the complex plane (Lapwood 1949; Miller and Pursey 1954). The discrete wave number (DWN) method (Bouchon and Aki 1977) takes advantage of practical discretization in wavenumber domain which allowed solving a variety of related problems (see e.g., Bouchon 2003).

The pioneering work by Aki (1957) on ambient seismic noise is at the core of significant developments. It has been found that the imaginary part of the elastodynamic Green's function is proportional to the average of the field correlations within a diffuse field (for recent reviews, see Weaver 2010 and Perton and Sánchez-Sesma 2016). A diffuse field develops within a system if there is illumination of elastic plane waves that fulfill the Principle of Equipartition (EQP) of Energy (Weaver 1982, 2010; Sánchez-Sesma and Campillo 2006; Sánchez-Sesma et al. 2006; Perton et al. 2009; Margerin et al. 2009). On the other hand, even simple illumination of isolated sources may give rise to diffuse fields after multiple scattering takes place (see Hennino et al. 2001; Campillo and Paul 2003; Paul et al. 2005). Plane waves illumination may be constructed to represent the contributions of a diffuse field, and the use of correlations to compute Green's function is well established (see Weaver 1984, 1985; Weaver and Lobkis 2001; Wapenaar 2004; van Manen et al. 2005; Sánchez-Sesma and Campillo 2006; Sánchez-Sesma et al. 2006; Pérez-Ruiz et al. 2008; Perton et al. 2009). The connection between this deterministic problem, namely, the computation of elastic Green's function and the diffuse field theory has been pointed out by Sánchez-Sesma et al. (2011) in the framework of the partition of the energy injected into a half-space by surface loads (see Miller and Pursey 1955 and Weaver 1985). The Green's functions retrieval for layered systems was formulated by Margerin (2009) invoking a cocktail of equipartitioned body (*P*, *SV*, *SH*) and surface waves (Rayleigh and Love). Sánchez-Sesma et al. (2016) considered the exact solution for a 3D acoustic layer. On the other hand, Perton and Sánchez-Sesma (2016) studied the 2D case of a layered medium, while Baena-Rivera et al. (2016) considered a 2D alluvial basin. These are examples of synthetic diffuse fields.

In this work, we present a novel representation of the imaginary part of Green's tensor in an elastic half-space in terms of a set of incident homogeneous plane *P*, *SV* and *SH* waves, with incident angles uniformly distributed in the associated half sphere, including their reflected consequences, and azimuthally distributed plane Rayleigh waves. These wave packages are called here states and form a set of wave solutions of dynamic elasticity that together fulfill the Principle of Equipartition (EQP). This approach allows for direct summations of spatial contributions from the illumination fields, that exhibit the intrinsic orthogonality of all the states that compose a diffuse field and they come out to be deterministic ingredients of the Green's function. In this case, the synthetic diffuse field is in fact a homogeneous and inhomogeneous plane wave expansion.

What we present is not a new method; we just apply formally the used approach in the retrieval of Green's function by averaging cross-correlations of ambient noise wavefields which is assumed to be a diffuse field. After revising all the conditions, we consider the simplest problem in which we may construct a synthetic diffuse field using plane waves for both body and surface Rayleigh waves as well. We do not know if such a construct is unique. This is an open question. Theory asserts that point sources of mono-polar or multi-polar types can be used instead, but the advantage of plane waves in the half space is that the free-surface boundary conditions can be analytically enforced from the beginning. For horizontally layered media the approach requires including all the modal structures of Love and Rayleigh waves. This has been explored in 2D by Perton and Sánchez-Sesma (2016). The generation of a synthetic diffuse field may be possible for heterogeneous media using numerical methods like spectral-finite elements or finite differences and the issue was explored by van Manen et al. (2006).

The elastodynamic Green's function of the half-space has elicited fundamental research for more than a century. It is, no doubt, a classical problem and we do

consider it a great accomplishment to have a new solution. Beyond the beauty of this discovery, which includes the classical Lamb (1904) or Chao (1960) problems as particular cases, the interest of this research lies in the possibility of finding robust indicators of the diffuse nature of a given field from actual records of noise, microtremors or coda waves. Certainly, both EQP and DWN approaches become demanding for high frequencies or large distances in terms of wavelengths. Here, we present all the necessary steps to have a novel representation of Green's function. A subject that may emerge is the optimal illumination for a given source-receiver configuration. The new closed solution has still to be studied to clarify its advantages and limitations. It could be useful to generate adequate solutions for near source elastic field in layered medium. On the other hand, having indicators of the diffusive nature of a given field may be quite useful to assess the reliability of estimates of Green's functions. Having trustworthy diagnostics requires carefully planned experiments (see Hennino et al. 2001; Margerin et al. 2009 and Piña-Flores et al. 2021) and having a synthetic diffuse field may be valuable to devise a set of tests. Studying irregular wave guides, we found that the energy densities may be highly localized in space. This suggests it is better to use point sources instead of plane waves. Finally, this work clarifies the theoretical considerations for constructing synthetic diffuse fields as a preliminary step for studying their properties and identifying them in nature (see e.g., Piña-Flores et al. 2021). These subjects are part of our current research.

Green's function retrieval in full space

One of the simplest synthetic diffuse field can be constructed in the 3D full space. Such a field is given by isotropic illumination of elastic body *P, SV* and *SH* plane waves whose amplitudes fulfill the Principle of Equipartition (see Sánchez-Sesma and Campillo 2006). In general, one can retrieve the elastodynamic Green's function in frequency domain from averaging cross-correlations of a diffuse field (Sánchez-Sesma et al. 2008):

$$\left\langle u_i(\mathbf{x}_\mathrm{A},\omega)u_j^*(\mathbf{x}_\mathrm{B},\omega)\right\rangle = -2\pi\xi_S k^{-3}\mathrm{Im}\left[G_{ij}(\mathbf{x}_\mathrm{A},\mathbf{x}_\mathrm{B},\omega)\right], \tag{1}$$

where $u_i(\mathbf{x},\omega)=$ Fourier transform of displacement in direction i at point $\mathbf{x}$, $\omega=$angular frequency, the star means complex conjugate, $\xi_S=$ shear waves average energy density of the isotropic background field (includes *SH* and *SV* waves because $\xi_{SH}=\xi_{SV}=\xi_S/2$), $k=\omega/\beta$ shear wavenumber, $\beta=$shear wave speed and $G_{ij}(\mathbf{x}_\mathrm{A},\mathbf{x}_\mathrm{B},\omega)=$ Green's function which is defined as the displacement at $\mathbf{x}_\mathrm{A}$ in direction i produced by a unit harmonic point force at $\mathbf{x}_\mathrm{B}$ in direction j. In this equation, angle brackets denote ensemble average which in 3D full-space means uniform angular averaging over the sphere. The derivation of Eq. 1 and some remarks on the orthogonality of wave states is given in Appendix 1. Consider that source and receiver coincide, $\mathbf{x}_\mathrm{A}=\mathbf{x}_\mathrm{B}=\mathbf{x}$, the left-hand side of Eq. 1 is the average of spectral density or auto-correlation. Assuming $i=j=1$, we can define from Eq. 1 the directional energy density in direction 1 by means of

$$\xi_1(\mathbf{x},\omega)=\rho\omega^2\left\langle u_1(\mathbf{x},\omega)u_1^*(\mathbf{x},\omega)\right\rangle = -2\pi\mu\xi_S k^{-1}\mathrm{Im}\left[G_{11}(\mathbf{x},\mathbf{x},\omega)\right]. \tag{2}$$

Here, $\mu=\rho\beta^2=$ Lamé's shear modulus, and $\rho=$mass density. In the far right-hand expression, we see the imaginary part of Green's function at the source. It is not singular and represents the radiated energy into the medium by a unit harmonic load. From Stokes' (1849) solution, the imaginary part of Green's function $G_{11}(\mathbf{x},\mathbf{x},\omega)$ for a homogeneous, unbounded medium is

$$\mathrm{Im}\left[G_{11}(\mathbf{x},\mathbf{x},\omega)\right]=-\frac{\omega}{12\pi\rho}\left(\frac{1}{\alpha^3}+\frac{2}{\beta^3}\right). \tag{3}$$

In Eq. 3, $\alpha=$dilatational wave velocity. While the real part diverges, the imaginary part is smooth in space and has a linear dependence on frequency ω. It accounts for the energy injected into the medium by the unit harmonic load (see Weaver 1985; Sánchez-Sesma et al. 2008).From Eqs. 2 and 3, we can identify that the directional energy density is one-third of total energy, that is to say, $\xi_1=\xi_P/3+\xi_S/3$. In a full space the average cross-correlation of P and S waves is null. Moreover, using a mode counting approach Weaver (1982) found that $\xi_S/\xi_P=2\alpha^3/\beta^3$, which is connected with the proportions that stem from the single load result of Eq. 3. As the energy of shear waves splits equally into the two polarizations, it is possible to write that $\xi_P+\xi_{SV}+\xi_{SH}=\xi=$ total energy density. If $R=\alpha/\beta$, this can be written as:

$$\xi_P=(1+2R^3)^{-1}\xi, \xi_{SV}=R^3(1+2R^3)^{-1}\xi, \xi_{SH}=R^3(1+2R^3)^{-1}\xi. \tag{4}$$

Equations 1, 2, 3 and 4 have been deduced from relationships valid for an unbounded homogeneous and elastic domain. They relate the average cross-correlations with elastodynamic Green's function and allow for a clear understanding of the nature of equipartition. These energy densities are associated to the illumination. We assume that this is a uniform background radiation. Within an inhomogeneous region (with layers, inclusions and voids, for instance) connected with the space in which the uncorrelated sources of illumination are established, the engendered field are related with the Green's function with the same equations. Equipartition

is needed for the illumination, enriched by the scattered consequences (see e.g., Sánchez-Sesma et al. 2006; 2008).

Green's function retrieval in half-space

The 3D elastic half-space also allows for the analytical construction of the required equipartitioned states. In this case, the free surface guides the propagation of non-dispersive, Rayleigh waves. Thus, the EQP cocktail of states of the plane P and S waves with their reflected consequences is enlarged with the uniform illumination of the Rayleigh waves. For a half-space only one Rayleigh plane wave exists. Given a region in the flat free-surface, the various directions imply states that can be easily counted thanks to the fact that vertical motion for non-dispersive Rayleigh waves satisfies in any horizontal plane the scalar 2D wave equation. Once the density of states is established, the proportionality constant for the energy is the same as the one for deep space. Following Weaver (1982), the energy density per unit area is $\xi_R = \pi\beta^2(2c_R^2 k)^{-1}\xi_S$, where c_R=wave speed of Rayleigh waves. Using Eq. 4, the Rayleigh energy density can be given in terms of the total energy density in deep space:

$$\xi_R = \frac{\pi\beta}{\omega}\left(\frac{\beta}{c_R}\right)^2 \frac{R^3}{1+2R^3}\xi. \tag{5}$$

Equation 5 is specific for the homogeneous half-space where only one plane wave Rayleigh mode exists. It allowed Perton et al. (2009) to compute the energy densities within an elastic half-space. They considered incidence of an equipartitioned set of elastic waves and displayed energy densities against depth, for both wave states and degrees of freedom. Naturally, the corresponding sums of energies came out to be the same. That showed the two faces of equipartition.The energy density for shear waves at the illumination level (deep half-space) is $\xi_S = \rho\omega^2 S^2(\omega)$, where $S^2(\omega)$ = spectral density of shear waves, here it is assumed unit. From Eq. 1 we have:

$$\mathrm{Im}\left[G_{ij}(\mathbf{x}_\mathrm{A},\mathbf{x}_\mathrm{B},\omega)\right] = -\frac{\omega}{2\pi\rho\beta^3}\left\langle u_i(\mathbf{x}_\mathrm{A},\omega)u_j^*(\mathbf{x}_\mathrm{B},\omega)\right\rangle. \tag{6}$$

The ensemble average of the cross-correlation is taken here as an interior or scalar product and is consistent with the notion of states that form a continuous orthogonal basis with the same statistics of normal modes (see Margerin 2009). This notable property implies that the only contributions to Green's function come from the cross-correlations of each state alone. For the half-space, Eq. 6 is written as:

$$\begin{aligned}
\mathrm{Im}\left[G_{ij}(\mathbf{x}_\mathrm{A},\mathbf{x}_\mathrm{B},\omega)\right] &= \frac{A}{2\pi}\int_0^{2\pi}\int_0^{\pi/2} u_i^P(\mathbf{x}_\mathrm{A},\theta,\phi,\omega)u_j^{P*}(\mathbf{x}_\mathrm{B},\theta,\phi,\omega)\sin\theta\, d\theta d\phi + \\
&+\frac{AR^3}{2\pi}\int_0^{2\pi}\int_0^{\pi/2} u_i^{SV}(\mathbf{x}_\mathrm{A},\theta,\phi,\omega)u_j^{SV*}(\mathbf{x}_\mathrm{B},\theta,\phi,\omega)\sin\theta\, d\theta d\phi + \\
&+\frac{AR^3}{2\pi}\int_0^{2\pi}\int_0^{\pi/2} u_i^{SH}(\mathbf{x}_\mathrm{A},\theta,\phi,\omega)u_j^{SH*}(\mathbf{x}_\mathrm{B},\theta,\phi,\omega)\sin\theta\, d\theta d\phi + \\
&+\frac{AR^3}{2\pi}\times\frac{2\pi\delta^2}{I_0}\int_0^{2\pi} u_i^R(\mathbf{x}_\mathrm{A},\phi,\omega)u_j^{R*}(\mathbf{x}_\mathrm{B},\phi,\omega)d\phi,
\end{aligned} \tag{7}$$

where $u_i^P(\mathbf{x},\theta,\varphi,\omega)$= full displacement field associated to an incoming plane P wave with azimuth φ and incidence angle θ with respect to the vertical axis$x_3 = z$, including its reflections. Figure 1 shows the systems of reference and the incidence of a homogeneous plane wave with forward azimuth ϕ measured from the x-axis as well as the polarization of P, SV and SH waves. In these integrals the common factor $A = \left\{-k(2\pi\mu)^{-1}\right\}\left(1+2R^3\right)^{-1}\xi/\rho\omega^2$, $\delta = \beta/c_R$, c_R=velocity of Rayleigh waves and I_0 = integral for normalization purposes that will be defined later. The brackets in the first part of A include the factor in Eq. 7 while the second factor gives the normalized energy density of P waves. In what follows, the normalized energy of the illumination $\xi/\rho\omega^2$ is assumed unity.

The contribution of P waves

Here, we express the complete displacement field generated by the incidence of a plane P wave from deep space, which is given by $u_i^{P0}(\mathbf{x},\theta,\phi,\omega) = P(\omega)n_i\exp(-\mathrm{i}\omega n_q x_q/\alpha)\exp(\mathrm{i}\omega t)$, where$n_1 = \sin\theta\cos\varphi$, $n_2 = \sin\theta\sin\varphi$ and $n_3 = -\cos\theta$,

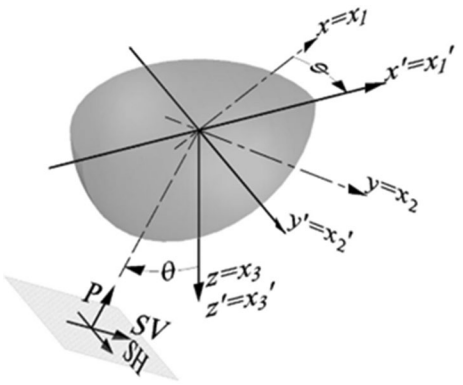

Fig. 1 Systems of reference. The 3D reference system is the Cartesian one *x*, *y* and *z* for the horizontal axis and the downward vertical one, respectively. The half-space corresponds to $z \geq 0$. It is common use in the text and elsewhere that $x = x_1$, $y = x_2$ and $z = x_3$. This sketch shows the incidence of a generic homogeneous plane wave with incidence angle θ with respect to the vertical and forward azimuth φ measured from the *x*-axis. The angle θ is measured from *z*-axis within the plane (x', z'). Only to illustrate the polarization, the thick arrows show positive particle motion of the incoming *P*, *SV* and *SH* waves. Particle motion polarization vectors for incident and reflected waves are given in the text

$P(\omega)$ = particle motion of incident *P* wave. Note that vector $\boldsymbol{n}$ gives both the wave polarization and the propagation direction. Also, the expression $n_q x_q = n_1 x_1 + n_2 x_2 + n_3 x_3$ is the internal product $\boldsymbol{n} \cdot \boldsymbol{x}$ which defines the propagation coordinate. It implies the summation convention (see e.g., Aki et al. 2002). With the free surface at $x_3 = z = 0$ there will be reflected *P* and *SV* waves. Assuming $P(\omega) = 1$, because energy partitions are already considered, we have

$$\begin{aligned} u_i^P(\mathbf{x},\omega) &= n_i \exp(-\mathrm{i}\omega n_q x_q/\alpha) \\ &+ n_i^{PP} PP \exp(-\mathrm{i}\omega n_q^{PP} x_q/\alpha) \\ &+ m_i^{PS} PS \exp(-\mathrm{i}\omega n_q^{PS} x_q/\beta). \end{aligned} \tag{8}$$

Here and hereafter the factor $e^{i\omega t}$ is omitted. Also $n_1^{PP} = \sin\theta\cos\phi$, $n_2^{PP} = \sin\theta\sin\phi$ and $n_3^{PP} = \cos\theta$. For reflected *S* wave the Snell's law implies $\sin\theta' = \beta/\alpha \sin\theta$ and $n_1^{PS} = \sin\theta'\cos\varphi$, $n_2^{PS} = \sin\theta'\sin\varphi$, and $n_3^{PS} = \cos\theta'$. The polarization vector for reflected *S* waves is given by $m_1^{PS} = \cos\theta'\cos\varphi$, $m_2^{PS} = \cos\theta'\sin\varphi$, and $m_3^{PS} = -\sin\theta'$. The corresponding reflection coefficients *PP*, *PS* are given in Appendix 2 in terms of incidence and reflection angles.

The contribution of SV waves

Similarly, as in the previous case, for the *SV* state we have

$$\begin{aligned} u_i^{SV}(\mathbf{x},\omega) &= m_i \exp(-\mathrm{i}\omega n_q x_q/\beta) \\ &+ n_i^{SP} SP \exp(-\mathrm{i}\omega n_q^{SP} x_q/\alpha) \\ &+ m_i^{SS} SS \exp(-\mathrm{i}\omega n_q^{SS} x_q/\beta), \end{aligned} \tag{9}$$

where $n_1 = \sin\theta\cos\varphi$, $n_2 = \sin\theta\sin\varphi$, $n_3 = -\cos\theta$, $m_1 = \cos\theta\cos\varphi$, $m_2 = \cos\theta\sin\varphi$, and $m_3 = \sin\theta$. Vectors *n* and *m* give the propagation direction and the wave polarization, respectively. They are orthogonal. Reflected *S* waves keep their horizontal slowness; therefore, $n_1^{SS} = \sin\theta\cos\varphi$, $n_2^{SS} = \sin\theta\sin\varphi$, and $n_3^{SS} = \cos\theta$ and the polarization is given by $m_1^{SS} = \cos\theta\cos\varphi$, $m_2^{SS} = \cos\theta\sin\varphi$, and $m_3^{SS} = -\sin\theta$. For reflected *P* wave Snell's law implies $\sin\theta' = \alpha/\beta \sin\theta$ and therefore the propagation is given by $n_1^{SP} = \sin\theta'\cos\varphi$, $n_2^{SP} = \sin\theta'\sin\varphi$, and $n_3^{SP} = \cos\theta'$. Here $\cos\theta' = +\sqrt{1-(\alpha/\beta)^2\sin^2\theta}$ may become imaginary for incidence angles beyond the critical angle. In that case, it suffices that $\cos\theta' = -\mathrm{i}\sqrt{(\alpha/\beta)^2\sin^2\theta - 1}$ which implies exponential attenuation with depth. The corresponding reflection coefficients *SP* and *SS* are given in Appendix 2.

The contribution of SH waves

The *SH* case is much simpler as there is no mode conversion and the reflection coefficient is unit. Therefore, we can write:

$$u_i^{SH}(\mathbf{x},\omega) = h_i \exp(-\mathrm{i}\omega\, n_q x_q/\beta) + h_i \exp(-\mathrm{i}\omega\, n_q^{SS} x_q/\beta), \tag{10}$$

where $h_1 = -\sin\varphi$, $h_2 = \cos\varphi$, $h_3 = 0$, $n_1 = \sin\theta\cos\varphi$, $n_2 = \sin\theta\sin\varphi$, and $n_3 = -\cos\theta$.

The contribution of Rayleigh waves

For Rayleigh waves, the energy density per unit area is given by Eq. 5. Considering that the energy of these incoming surface waves per unit volume varies with depth, we follow Weaver (1985) and Perton et al. (2009), using a somewhat modified notation, and write:

$$\begin{aligned} \xi_R &= \frac{1}{2\pi}\int_0^{2\pi}\int_0^{\infty} \rho\omega^2 \left\{ \left|u_x^R\right|^2 \cos^2\phi + \left|u_y^R\right|^2 \sin^2\phi + \left|u_z^R\right|^2 \right\} dz d\phi \\ &= \int_0^{\infty} \rho\omega^2 \left\{ \left|u_x^R(0,z,\omega)\right|^2 + \left|u_z^R(0,z,\omega)\right|^2 \right\} dz. \end{aligned} \tag{11}$$

The displacements of a Rayleigh wave are given by

$$u_x^R(x,z,\omega) = B\left[2\delta^2\exp(-\gamma z) + (1-2\delta^2)\exp(-\nu z)\right]\exp(-\mathrm{i}k_R x), \text{ and}$$
$$u_z^R(x,z,\omega) = \mathrm{i}\zeta B\left[(1-2\delta^2)\exp(-\gamma z) + 2\delta^2\exp(-\nu z)\right]\exp(-\mathrm{i}k_R x), \tag{12}$$

where B=amplitude of horizontal displacement, $\delta = \beta/c_R$, c_R=velocity of Rayleigh waves, $k_R = \omega/c_R =$ horizontal wavenumber, $\gamma = (\omega/\alpha)\sqrt{(\alpha/c_R)^2 - 1}$, $\nu = (\omega/\beta)\sqrt{\delta^2 - 1}$ are the vertical wavenumbers of P and S waves and $\zeta = (2\delta^2 - 1)/2\delta\sqrt{\delta^2 - 1} =$ ellipticity. After performing the integrals in Eq. 11 and considering Eq. 6 we can write

$$B^2 = \frac{2\pi}{I_0}\delta^2\frac{R^3}{1+2R^3}\frac{\xi}{\rho\omega^2}, \tag{13}$$

where $I_0 = (4\delta^4 + \zeta^2 b^2)/2r + (b^2 + 4\zeta^2\delta^4)/2s + (4b\delta^2 d)/(r+s)$, $b = 1 - 2\delta^2$, $d = 1 + \zeta^2$, $r = \sqrt{\delta^2 - \beta^2/\alpha^2}$ and $s = \sqrt{\delta^2 - 1}$.

Discretization

The angular integrals of Eq. 7 are discretized to cover the illumination from the half-space. In Eq. 14 the displacements of incoming P, SV and SH waves should be represented with the expressions given in Eqs. 8–10. Rayleigh waves, which are described in Eq. 12, are included here with $B=1$ because Eq. 14 already accounts for the normalization of Eq. 13:

$$\begin{aligned}
\mathrm{Im}\left[G_{ij}(\mathbf{x}_\mathrm{A},\mathbf{x}_\mathrm{B},\omega)\right] \approx{}& \frac{A}{2\pi}\sum_{m=1}^{N_\phi}\sum_{n=1}^{N_\theta} u_i^P(\mathbf{x}_\mathrm{A},\theta_n,\phi_m,\omega)u_j^{P*}(\mathbf{x}_\mathrm{B},\theta_n,\phi_m,\omega)\sin\theta_n\Delta\theta\Delta\phi + \\
&+\frac{AR^3}{2\pi}\sum_{m=1}^{N_\phi}\sum_{n=1}^{N_\theta} u_i^{SV}(\mathbf{x}_\mathrm{A},\theta_n,\phi_m,\omega)u_j^{SV*}(\mathbf{x}_\mathrm{B},\theta_n,\phi_m,\omega)\sin\theta_n\Delta\theta\Delta\phi + \\
&+\frac{AR^3}{2\pi}\sum_{m=1}^{N_\phi}\sum_{n=1}^{N_\theta} u_i^{SH}(\mathbf{x}_\mathrm{A},\theta_n,\phi_m,\omega)u_j^{SH*}(\mathbf{x}_\mathrm{B},\theta_n,\phi_m,\omega)\sin\theta_n\Delta\theta\Delta\phi + \\
&+\frac{AR^3}{2\pi}\times\frac{2\pi\delta^2}{I_0}\sum_{m=1}^{N\phi} u_i^R(\mathbf{x}_\mathrm{A},\phi_m,\omega)u_j^{R*}(\mathbf{x}_\mathrm{B},\phi_m,\omega)\Delta\phi.
\end{aligned} \tag{14}$$

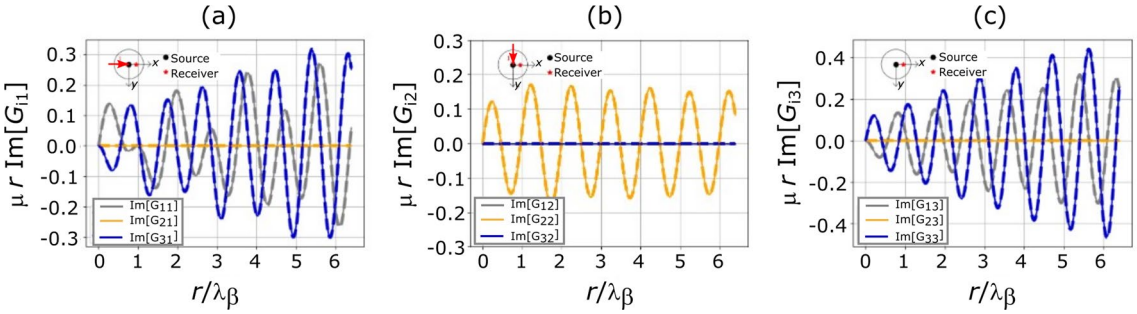

Fig. 2 Comparison of imaginary part of the Green functions for the case of source and receivers at the surface of an elastic Poissonian half-space. The source is at the origin $(0, 0, 0)^\mathrm{T}$ and the receivers are located along x-axis at $(r, 0, 0)^\mathrm{T}$, where r=horizontal distance. Results computed using EQP are depicted with discontinuous lines while the continuous lines correspond to DWN. Results display the non-dimensional Green's function components $\mu r\mathrm{Im}[G_{ij}]$ against the normalized distance r/λ_β, where $\lambda_\beta = \beta/f =$ shear wavelength. The first two plots correspond Chao's problem while the third one to G_{i3} Lamb's. Gray, yellow and blue lines represent motion in x, y and z directions, respectively

Numerical results

In order to establish the goodness of this approach, we compare the EQP results for point loads at the surface of half-space with those obtained with direct computation of wavenumber integrals. For harmonic forcing, Lamb's (1904) and Chao's (1960) problems have integral representations, in the frequency-horizontal wavenumber domain, in terms of exponentials and Bessel functions for depth and radial dependence. Moreover, sines and cosines appear for azimuthal dependence in the tangential load case. For a vertical load the Green function of Lamb's problem for radial component can be written as:

$$G_{r3}(r,z,\omega) = \frac{1}{2\pi\mu}\int_0^\infty \frac{\left(k^2-\nu^2\right)\exp(-i\gamma z)+2\gamma\nu\exp(-i\nu z)}{\left(k^2-\nu^2\right)^2+2\gamma\nu k^2} k^2 J_1(kr)dk, \tag{15}$$

while the vertical component is

$$G_{z3}(r,z,\omega) = \frac{i}{2\pi\mu}\int_0^\infty \frac{\left(k^2-\nu^2\right)\exp(-i\gamma z)-2k^2\exp(-i\nu z)}{\left(k^2-\nu^2\right)^2+2\gamma\nu k^2}\gamma k J_0(kr)dk, \tag{16}$$

where the vertical wavenumbers are $\gamma=\sqrt{\omega^2/\alpha^2-k^2}$ and $\nu=\sqrt{\omega^2/\beta^2-k^2}$, with their imaginary parts being null or negative, $J_m(kr)$ is Bessel function of the first kind and order m, r = radial coordinate and k = radial horizontal wavenumber.For the horizontal load along x_1, the Chao (1960) solution can be written as (omitting the argument kr in the Bessel functions):

$$G_{r1}(r,z,\omega) = \frac{-i}{2\pi\mu}\cos\varphi\int_0^\infty \frac{2k^2\exp(-i\gamma z)-\left(k^2-\nu^2\right)\exp(-i\nu z)}{\left(k^2-\nu^2\right)^2+2\gamma\nu k^2}k\nu(J_0-J_1/kr)dk+\frac{-i}{2\pi\mu}\cos\varphi\int_0^\infty \frac{\exp(-i\nu z)}{\nu}k(J_1/kr)dk, \tag{17}$$

$$G_{\varphi1}(r,z,\omega) = \frac{i}{2\pi\mu}\sin\varphi\int_0^\infty \frac{2k^2\exp(-i\gamma z)-\left(k^2-\nu^2\right)\exp(-i\nu z)}{\left(k^2-\nu^2\right)^2+2\gamma\nu k^2}k\nu(J_1/kr)dk+\frac{i}{2\pi\mu}\sin\varphi\int_0^\infty \frac{\exp(-i\nu z)}{\nu}k(J_0-J_1/kr)dk, \tag{18}$$

and

$$G_{z1}(r,z,\omega) = \frac{-1}{2\pi\mu}\cos\varphi\int_0^\infty \frac{2\gamma\nu\exp(-i\gamma z)+\left(k^2-\nu^2\right)\exp(-i\nu z)}{\left(k^2-\nu^2\right)^2+2\gamma\nu k^2}k^2 J_1 dk, \tag{19}$$

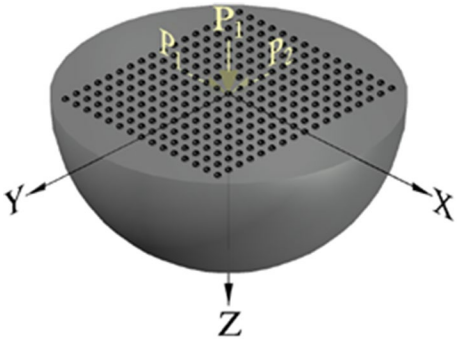

Fig. 3 Half-space loaded on the surface. Receivers covering a square with side of 20 shear wavelengths

for radial, transverse and vertical components, respectively. The first two components display the contributions of *P-SV* and *SH* waves in the corresponding wavenumber integrals. As it should be, the vertical component is due only to *P-SV* waves.

Equations 15–19 were used to validate our solution. They can be evaluated analytically using the Cauchy's residue theorem. The representations would be valid asymptotically for large distances. The issue is discussed in detail in several textbooks (e.g., Aki et al. 2002; Kausel 2006). For buried sources, equivalent expressions can be obtained. In this work, we used the DWN method to do the validations.

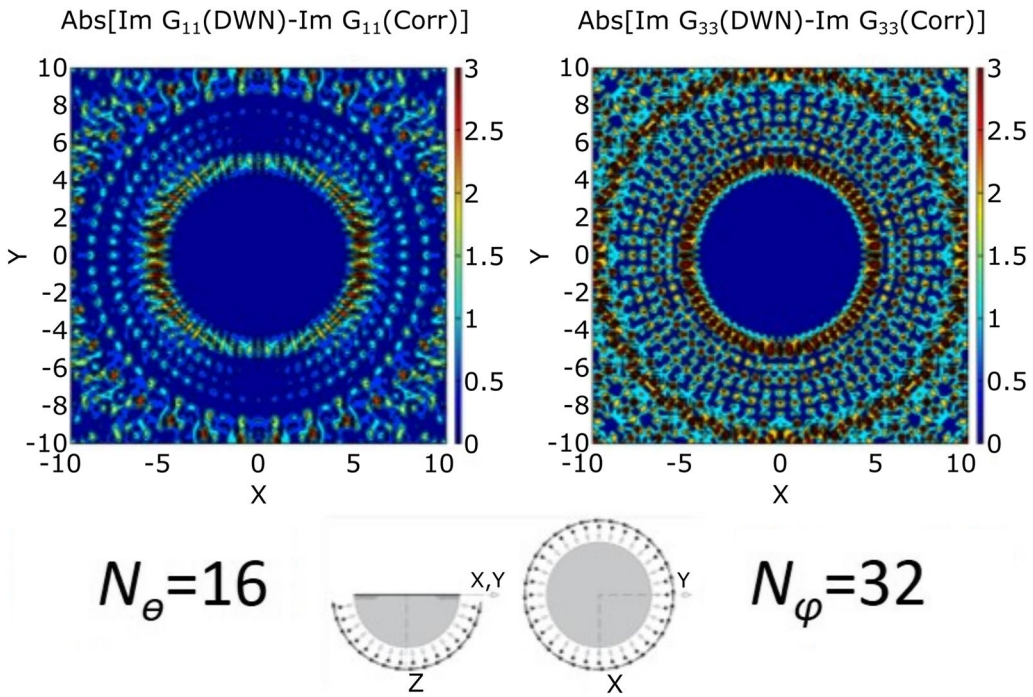

Fig. 4 Relative errors of surface results within a square for a horizontal and vertical unit harmonic forces, respectively. Illumination is given by $N_\theta = 16$ and $N_\varphi = 32$. The square side has 20 wavelengths

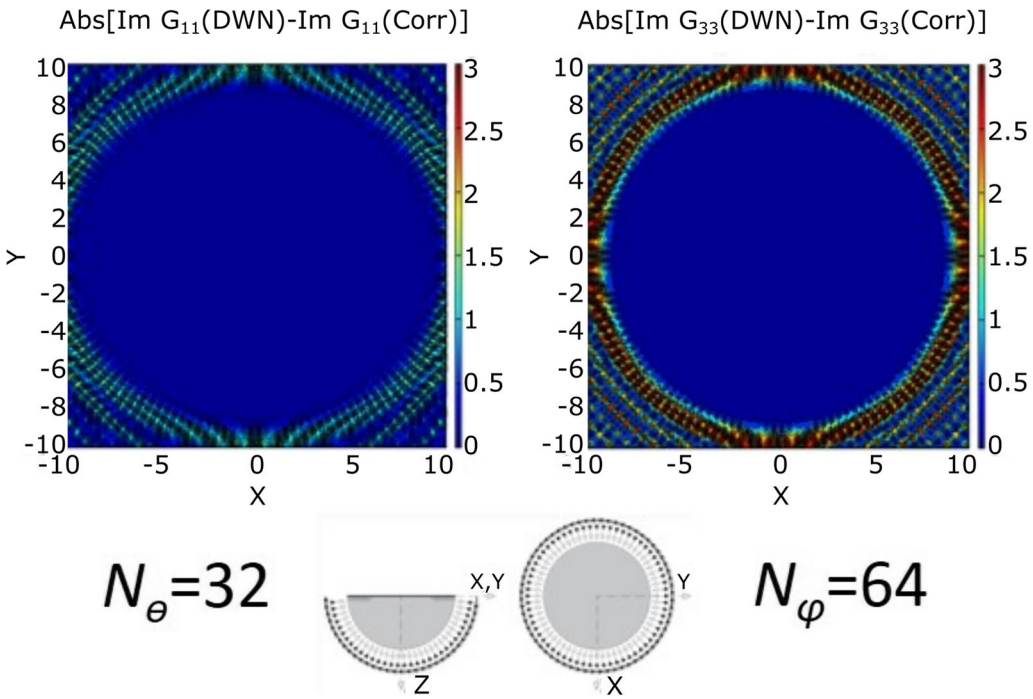

Fig. 5 Relative errors of surface results within a square for a horizontal and vertical unit harmonic forces, respectively. Illumination is given by $N_\theta = 32$ and $N_\varphi = 64$. The square side has 20 wavelengths

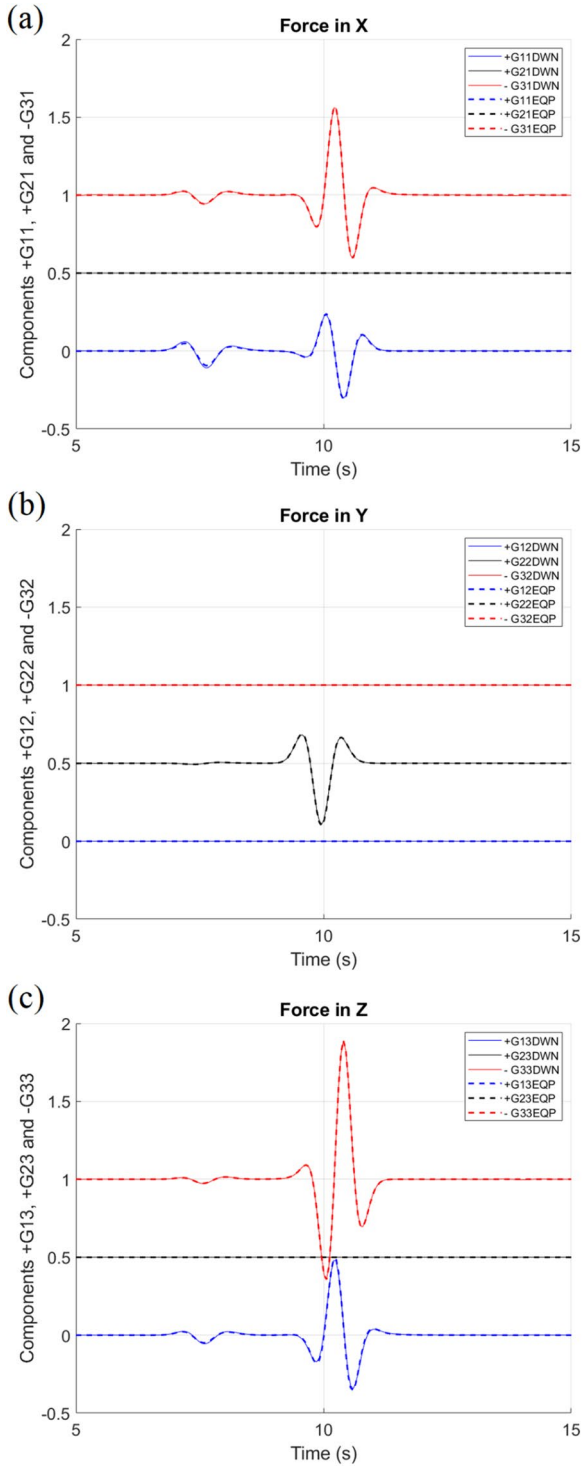

Fig. 6 Synthetic seismograms are given in the panels a, b and c for the three forces in directions *x*, *y* and *z*, respectively, at the origin and the receiver at $x_1 = 5$ km both on the surface of a half-space with Poisson ratio of 1/3. The *P* and *S* wave velocities are 2 and 1 km/s, respectively. Mass density is 2×10^3 kg/m^3. The chosen source was a Ricker pulse with "characteristic" period of 1 s and centered at 5 s. The maximum load value in absolute value is R_0 in *GN* (10^9*Newtons*). Results from DWN are given with continuous lines as indicated in the legends. The synthetics using EQP are superimposed with dotted thick lines. The ordinates' unit is meters after the common factor $2\pi 10^4 R_0^{-1}$ is applied

The solution with EQP is simply obtained by computing Eq. 14 for the given positions of points $\mathbf{x}_A$ and $\mathbf{x}_B$ for a desired frequency ω. The density of angular discretization of the associated half sphere is controlled by N_ϕ and N_θ (as a rule of thumb, the sum of angular discretizations should give 2π for both the double sum and the single one, $\Delta\phi = 2\pi/N_\phi$ and $\Delta\theta = \pi/2N_\theta$). In Fig. 2a, b the results for the imaginary parts of the components $G_{i1}(\mathbf{x}, 0, \omega)$, and $G_{i2}(\mathbf{x}, 0, \omega)$ are presented for $\boldsymbol{\alpha}/\boldsymbol{\beta} = \sqrt{3}$ (Poisson's solid), where $i = 1$, 2 or 3. Figure 2c presents the results for a vertical load, with same configuration and material properties.

To gauge the influence of the angular discretization of the component plane waves, we compute the percent relative error of $\mathrm{Im}[G_{ij}]$ on the surface of the half-space. We study dynamic loads at the origin and receivers located within a square with side of 20 shear wavelengths as shown in Fig. 3. For instance, the error of vertical component is defined as:

$$\left(\left|\mathbf{Im}\left[G_{33}^{EQP}\right] - \mathbf{Im}\left[G_{33}^{DWN}\right]\right|/\mathbf{NORM}\right) \times 100, \quad (20)$$

where $\mathbf{NORM} = (\mathbf{Im}[G_{11}^{EQP}]^2 + \mathbf{Im}[G_{22}^{EQP}]^2 + \mathbf{Im}[G_{33}^{EQP}]^2)^{1/2}$ and similarly for the horizontal one. This normalization was chosen because the tensor trace is stable, although it may lead to some slight underestimation of error. Figure 4 displays the errors for $N_\theta = 16$ and $N_\phi = 32$, and relative errors are below 5 percent within a radius of five wavelengths. For $N_\theta = 32$ and $N_\phi = 64$, we display similar results in Fig. 5. For a denser illumination the relative error decreases significantly. The zone with errors less than 4 percent has a radius of about ten wavelengths. We computed the percent relative error of $\mathrm{Im}[G_{ij}]$ to gauge the influence of angular discretization on the average of the cross-correlations of the diffuse field constituents. The illumination is better in the neighborhood of the origin and explains why a finer angle coverage is better. This shows that the synthetic diffuse field properties degrade away from the origin. It would be interesting to evaluate the relative contributions of the various parts, but this is beyond the scope of this research. The derivations presented here have been performed in frequency domain. In what follows, some examples are given in time dom ain.

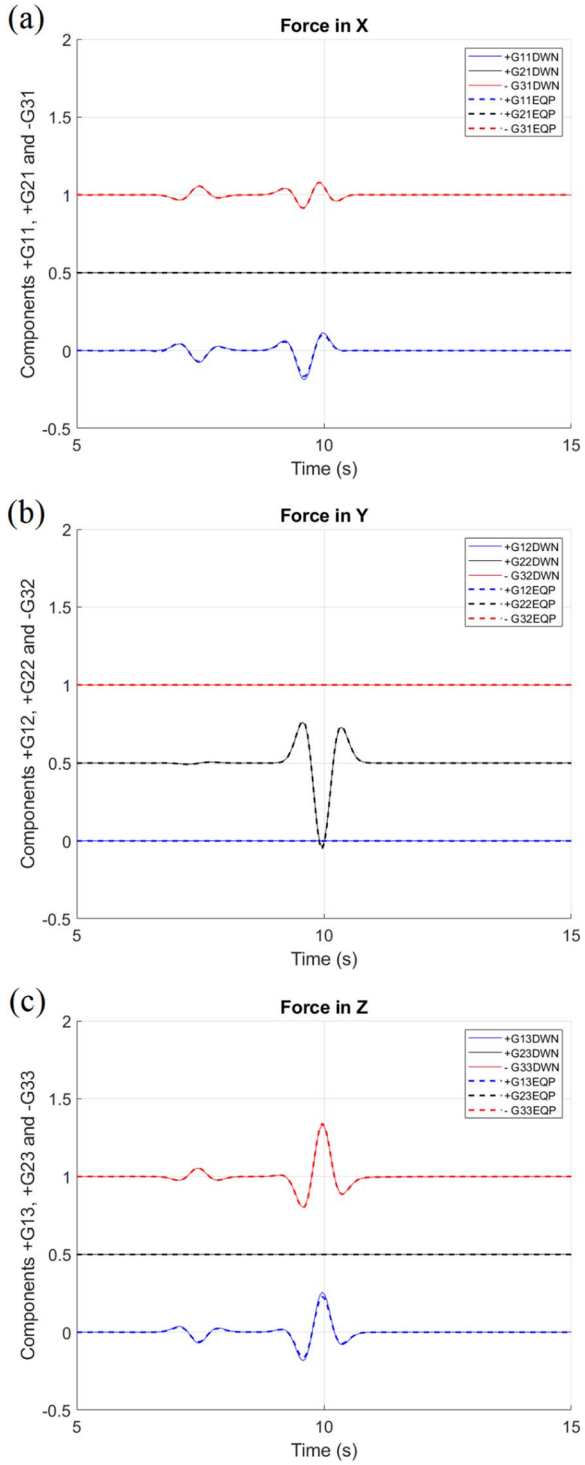

Fig. 7 Synthetic seismograms for the three forces at the origin and the receiver at $x_1 = 4$ km, $x_2 = 0$ and depth $x_3 = 3$ km. Both on the surface of a half-space with Poisson ratio of 1/3. The chosen source was a Ricker pulse with "characteristic" period of 1 s and centered at 5 s. The maximum load value in absolute value is R_0 in *GN* (10^9 *Newtons*). The three panels correspond to force along *x*, *y* and *z*, respectively. Results from DWN are given with continuous lines as indicated in the legends. The synthetics using EQP are superimposed with dotted lines. The ordinates' unit is meters after the common factor $2\pi\, 10^4 R_0^{-1}$ is applied

Time domain results

In order to show the performance of the new representation of the Green's Function using EQP, we show some results in which the real part of Green's function is computed as the Hilbert transform of the imaginary part, i.e., both the real and the imaginary parts form a Hilbert pair (Aki et al. 2002). Therefore, synthetic seismograms have been computed from EQP and DWN formulations. Two examples are displayed: (1) both source and receiver are at the free surface; (2) the source is at the free surface and the receiver is below it; and (3) both source and receiver are inside the half-space. We assume the *P* and *S* wave velocities to be $\boldsymbol{\alpha} = 2$ and $\boldsymbol{\beta} = 1$, respectively (in km/s), moreover mass density is assumed to be $\boldsymbol{\rho} = 2 \times 10^3 \mathbf{kg}/\mathbf{m}^3$. A Ricker pulse is assumed for the time variations of the forces. This widely used waveform is defined as $2\boldsymbol{R}_0\left(\boldsymbol{a}^2 - 0.5\right)\mathbf{exp}(-\boldsymbol{a}^2)$, where the normalized time is $\boldsymbol{a} = \boldsymbol{\pi}(\boldsymbol{t} - \boldsymbol{t_s})/\boldsymbol{t_p}$ with $\boldsymbol{t_s}$ = central time, $\boldsymbol{t_p}$ = "characteristic" period of pulse and $\boldsymbol{R}_0$ = maximum of the applied loads (in absolute value) in *GN* (Giga Newtons). Therefore, the units of seismograms are $(2\boldsymbol{\pi})^{-1}10^{-4}\boldsymbol{R}_0$ in meters.

For the first example, we choose the source point at the origin of coordinates at the half-space surface and value at $x_1 = 5$ km the displacement field (i.e., the Green's tensor components). Figure 6 shows the comparison of synthetic seismograms obtained with DWN and EQP of the Green's tensor convolved with a Ricker pulse. The three forces at the origin and the receiver at $x_1 = 5$ km, $x_2 = 0$, both on the surface of a half-space with Poisson ratio of 1/3. The *S* wave velocity is 1 km/s and the *P* wave velocity is 2 km/s. The Ricker pulse has a "characteristic" period of 1 s and centered at 5 s. For the plane wave illumination, the values $N_\theta = 45$ and $N_\phi = 193$ were considered. Seismograms show a very good agreement. The three components are shifted with baselines of 0, 0.5 and 1.0 (in the same units of displacements) for the components in *x*, *y* and *z*, respectively.

Consider now the receiver is at $\boldsymbol{x}_1 = 4$ km, $\boldsymbol{x}_2 = 0$ and depth $\boldsymbol{x}_3 = 3$ km. A value of $\boldsymbol{t_p} = 1$ s was selected. Again, Poisson ratio of 1/3. As in the previous example the *P* pulse arrives at 5/2 = 2.5 s after the central time $\boldsymbol{t_s}$. Figure 7 shows the comparison of synthetic seismograms obtained with DWN and EQP. Again the Green's function was convolved with a Ricker pulse. Here the *S* wave dominates as it arrives at 5/1 = 5.0 s after the central time. At this depth, the small effect of Rayleigh waves is

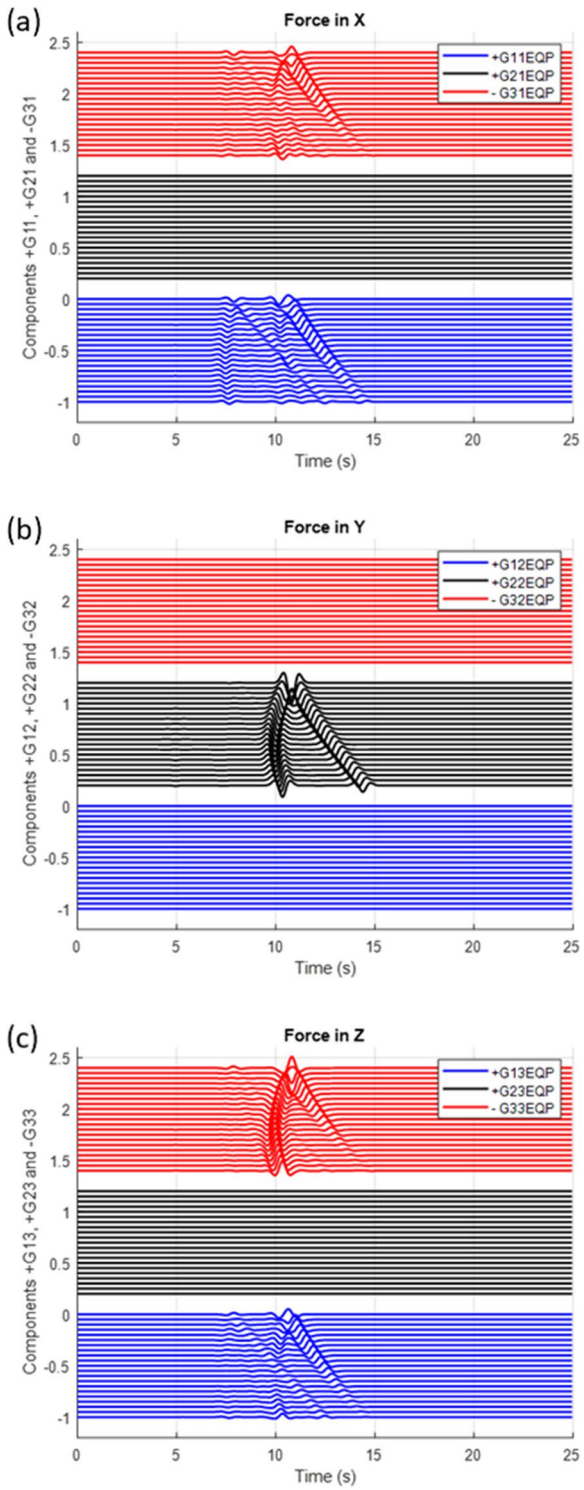

Fig. 8 The three panels depict the Green's function convolved with a Ricker pulse with $t_p = 1$ s and $t_s = 5$ s. The three forces (sources) are located at depth of $z = 3$ km and $x = y = 0$ and the receivers are 21 and are located at $x = 5$ km, $y = 0$ and depths equally distributed from $z = 0$ and 5 km, plotted in descending order from the free surface. The sign of vertical components (in red) has been changed. The ordinates' unit is meters after the common factor $2\pi\, 10^4 R_0^{-1}$ is applied

evident. The three components are shifted with baselines of 0, 0.5 and 1.0 (in the same units of displacements) for the components in x, y and z, respectively.

Some additional results are given for source and receivers at depth in Fig. 8. The three forces (sources) are located at depth of $z = 3$ km and $x = y = 0$ and the receivers are 21 at $x = 5$ km, $y = 0$ and depths equally distributed from $z = 0$ and 5 km, plotted in descending order from the free surface. The Green's function was convolved with a Ricker pulse with $t_p = 1$ s and $t_s = 5$ s. The simplest seismograms are those at the free-surface and the reflected consequences displaying mode conversions are clearly seen. In the transverse component, the hyperbolic move-outs of incident and reflected fields are depicted. The sign of vertical components (in red) has been changed so that polarities can be checked visually; i.e., the P waveforms in longitudinal and vertical components appear with similar shapes showing linear polarization. The amplitudes of the three components are shifted to baselines 0.0, 1.2 and 2.4 (in the same units of displacements).

Discussion and conclusions

This work stems from previous results (e.g., Sánchez-Sesma and Campillo 2006; Perton et al. 2009; Margerin 2009; Sánchez-Sesma et al. 2011; Perton and Sánchez-Sesma 2016). The 2D Green's function for the stratified half-space by Perton and Sánchez-Sesma (2016) requires the computation of dispersion curves and modal shapes which is far more involved than the canonical half-space problem presented herein. Our idea was to present this simpler case that allows a complete analytical solution. In this sense, these results extend those of Sánchez-Sesma and Campillo (2006). Therefore, we present here the solution of the canonical half-space Green's function retrieval problem.

We presented here a detailed procedure for the computation of the half-space elastodynamic Green's function in the frequency domain. The method relies on the Principle of Equipartition (EQP) of Energy. Theory asserts that the imaginary parts of Green's tensor is the average cross-correlations of the corresponding fields generated by the incidence of body and surface plane waves with relative amplitudes weighted by partition factors which constitute the recipe to construct a synthetic diffuse field. The half-space case is the simplest example in which surface waves appear. Rayleigh waves are a single-mode, non-dispersive waves so that the partition factor can be obtained analytically. Numerical results allow gauging the goodness of this approach. The errors are generally small but their spatial distributions suggest that there is room for improvement. What we obtained is essentially a proof of the concept.

The real part of the Green's function is the Hilbert transform of the imaginary one. Therefore, the complete half-space elastodynamic Green's function can be easily obtained. Moreover, time domain results display in all its grandeur the majestic Rayleigh waves and the excellent agreement with DWN calculations, clearly depicting our EQP solution as a new representation of frequency domain Green's function in terms of plane waves.

This communication may be helpful to clarify the theoretical considerations that lead to these fundamental results that are surprising for us who studied the classical Lamb's problem in its various forms. It is likely that integral transforms, after being recast as angular integrals, provide the obtained results as it happens for the simple 2D scalar case. However, doing so would be difficult and perhaps of little interest as we already have the exact solution. On the other hand, the optimization of this approach establishing for what sorts of geometries and circumstances might it be most useful is beyond the scope of this communication.

Diffuse fields are ubiquitous in nature. In most circumstances they arise as a consequence of the equilibration in multiple scattering regime that happens in the coda of earthquakes and also in a number of seismic ambient noise situations or even for localized sources in applications. Diffuse fields are intrinsically related to Green's functions. We are committed to identify then in reality. Therefore, understanding their properties may be useful in applications.

Appendices

Appendix 1

The retrieval of Green's function and the orthogonality of states

In a neighborhood of $\mathbf{x}_0$ with $\mathbf{x} = \mathbf{x}_0 + r\boldsymbol{e}_1$ and $\boldsymbol{e}_1 = (100)^T$, the Stokes (1849) solution for an impulse force $\delta(t)$(Dirac delta) in direction 1 can be written as:

$$G_{11}(\mathbf{x}, \mathbf{x}_0, t) = \frac{1}{4\pi\mu r}\left[\frac{\beta^2}{\alpha^2}\delta\left(t - \frac{r}{\alpha}\right) + 2\beta^2\int_{1/\alpha}^{1/\beta}\delta(t - sr)sds\right]. \tag{21}$$

For each Dirac delta (divided by r) we take the imaginary part of Fourier transform and the limit when r tends to zero:

$$\frac{\delta(t - sr)}{r} \to \mathrm{Im}\left[\frac{\exp(-i\omega sr)}{r}\right] \to \frac{-\sin(\omega sr)}{r} \to -\omega s. \tag{22}$$

Then, taking either the slowness s as α^{-1} or β^{-1} and $-\omega$ as a common factor, we have:

$$\mathrm{Im}[G_{11}(\mathbf{x}, \mathbf{x}, \omega)] = \frac{-\omega}{4\pi\mu}\left(\frac{\beta^2}{\alpha^2}\frac{1}{\alpha} + 2\beta^2\int_{1/\alpha}^{1/\beta}s^2ds\right) = \frac{-\omega}{12\pi\rho}\left(\frac{1}{\alpha^3} + \frac{2}{\beta^3}\right). \tag{23}$$

This can be generalized for the Green's tensor:

$$\mathrm{Im}\left[G_{ij}(\mathbf{x}, \mathbf{x}, \omega)\right] = \frac{-\omega}{12\pi\rho}\left(\frac{1}{\alpha^3} + \frac{2}{\beta^3}\right)\delta_{ij}, \tag{24}$$

where δ_{ij} = Kroenecker delta (=1 if i=j;=0 if $i \neq j$). Within an equipartitioned elastic field in a full space the ratio of energy densities of S and P waves, accounting for the two polarizations of S waves is $\xi_S/\xi_P = 2\alpha^3/\beta^3$ (Weaver 1982) and Eq. 23 can be written as:

$$\mathrm{Im}[G_{11}(\mathbf{x}, \mathbf{x}, \omega)] = \frac{-\omega}{6\pi\rho\beta^3}\left(1 + \frac{\beta^3}{2\alpha^3}\right) = \frac{-k}{6\pi\mu}\left(1 + \frac{\xi_P}{\xi_S}\right), \tag{25}$$

where $k = \omega/\beta$ = shear wavenumber and $\mu = \rho\beta^2$. As the energy density in direction one is $\xi_1 = \xi/3 = (\xi_S + \xi_P)/3 = \rho\omega^2\langle|u_1^2(\mathrm{x})|\rangle$ one has

$$\mathrm{Im}[G_{11}(\mathbf{x}, \mathbf{x}, \omega)] = \frac{-k}{6\pi\mu}\left(\frac{\xi_S + \xi_P}{\xi_S}\right) = \frac{-k}{2\pi\mu}\left(\frac{\rho\omega^2\langle|u_1^2(\mathrm{x})|\rangle}{\xi_S}\right), \tag{26}$$

where the brackets $\langle\cdot\rangle$ mean ensemble average. In this context, it can be expressed as:

$$\langle\cdot\rangle = \frac{1}{4\pi}\int_0^{2\pi}\int_0^{\pi}(\cdot)\sin\theta d\theta d\varphi, \tag{27}$$

where φ= azimuth and θ= co-latitude. Once the proportionality factors are set, we can write down the relationship with the adequate indexes:

$$\langle u_i(\mathbf{x}_A, \omega)u_j^*(\mathbf{x}_B, \omega)\rangle = -2\pi\xi_S k^{-3}\mathrm{Im}\left[G_{ij}(\mathbf{x}_A, \mathbf{x}_B, \omega)\right]. \tag{28}$$

This is Eq. 1 in the main text. In full space $u_i(\mathrm{x}, \omega)$ = Fourier transform of displacement in direction i at point x can be expressed in terms of P, SV and SH states:

$$u_i(\mathbf{x}, \omega) = u_i^P(\mathbf{x}, \omega) + u_i^{SV}(\mathbf{x}, \omega) + u_i^{SH}(\mathbf{x}, \omega). \tag{29}$$

Sánchez-Sesma and Campillo (2006) constructed the states as superposition of plane waves isotropically distributed with equipartitioned amplitudes. For a given frequency, the average cross-correlations are:

$$\begin{aligned}\langle u_i(\mathbf{x}_A)u_j^*(\mathbf{x}_B)\rangle \;=\; &\langle u_i^P(\mathbf{x}_A)u_j^{P*}(\mathbf{x}_B)\rangle + \langle u_i^{SV}(\mathbf{x}_A)u_j^{SV*}(\mathbf{x}_B)\rangle \\ &+ \langle u_i^{SH}(\mathbf{x}_A)u_j^{SH*}(\mathbf{x}_B)\rangle,\end{aligned} \tag{30}$$

which exhibits the orthogonality of body waves (Margerin 2009). In presence of scatterers and reflectors, the states are complemented with their corresponding diffracted and refracted consequences. Therefore, in the half-space, the ensemble average for body and surface waves states is given by:

$$\langle\cdot\rangle = \frac{1}{2\pi}\int_0^{2\pi}\int_0^{\pi/2}(\cdot)\sin\theta d\theta d\varphi, and \langle\cdot\rangle = \frac{1}{2\pi}\int_0^{2\pi}(\cdot)d\varphi, \tag{31}$$

respectively. In a layered half-space, the orthogonality of states includes body and surface waves (see Margerin 2009 and Perton and Sánchez-Sesma 2016). These results are related to Herrera's (1964) orthogonality relation for surface waves and Alsop's (1968) extension of such property to body waves.

Appendix 2

The corresponding reflection coefficients for incidence of homogeneous P and SV waves upon the half-space free surface can be found in Aki et al. (2002). Here, we summarize them.

Incident P plane waves

Due to the incidence of a plane P wave with incident angle θ, with respect to the vertical, both reflected P and SV plane waves with reflection angles θ and θ', respectively, are generated. Solving for null tractions at the free surface it is possible to obtain the reflection coefficients:

$$PP = \frac{-\left(\frac{1}{\beta^2}-2p^2\right)^2+4p^2\frac{\cos(\theta)}{\alpha}\frac{\cos(\theta')}{\beta}}{\left(\frac{1}{\beta^2}-2p^2\right)^2+4p^2\frac{\cos(\theta)}{\alpha}\frac{\cos(\theta')}{\beta}} \text{ and}$$

$$PS = \frac{4\frac{\alpha}{\beta}p\frac{\cos(\theta)}{\alpha}\left(\frac{1}{\beta^2}-2p^2\right)}{\left(\frac{1}{\beta^2}-2p^2\right)^2+4p^2\frac{\cos(\theta)}{\alpha}\frac{\cos(\theta')}{\beta}}, \quad \text{where} \quad p=\text{horizontal}$$

slowness which is given by: $p = \frac{\sin(\theta)}{\alpha} = \frac{\sin(\theta')}{\beta}$.

Incident SV plane waves

Assume now the incidence of a plane SV wave with incident angle θ, with respect to the vertical, that also produces both reflected SV and P plane waves with reflection angles θ and θ', respectively, are produced. Again, solving for null tractions at the free surface we obtain the reflection coefficients:

$$SP = \frac{4\frac{\beta}{\alpha}p\frac{\cos(\theta)}{\beta}\left(\frac{1}{\beta^2}-2p^2\right)}{\left(\frac{1}{\beta^2}-2p^2\right)^2+4p^2\frac{\cos(\theta')}{\alpha}\frac{\cos(\theta)}{\beta}} \text{ and}$$

$$SS = \frac{\left(\frac{1}{\beta^2}-2p^2\right)^2-4p^2\frac{\cos(\theta')}{\alpha}\frac{\cos(\theta)}{\beta}}{\left(\frac{1}{\beta^2}-2p^2\right)^2+4p^2\frac{\cos(\theta')}{\alpha}\frac{\cos(\theta)}{\beta}}, \quad \text{where} \quad p=\text{horizontal}$$

slowness, which is given by: $p = \frac{sin\theta'}{\alpha} = \frac{sin\theta}{\beta}$.

Acknowledgements

Thanks are given to M. Campillo and L. Margerin for enlightening discussions and their encouragement to complete this research; to J. C. Molina-Villegas, M. Baena-Rivera, E. Kausel, J. Piña-Flores, L. Rivera and R. L. Weaver for their critical reading of manuscript and useful remarks. The comments from two unknown reviewers and the Editor H. Kawase were helpful to improve the manuscript. Our appreciation to J. E. Plata and G. Sánchez and their team of USI at II-UNAM for locating useful references.

Author contributions

FJS-S conceived the main ideas and drafted the work. FJS-S and MP and FL created or revised software for seismogram computations. MAS-C and CAS-A prepared software for the representation of results and made several figures. AG-J and FL reviewed the draft and prepared the submitted version of the manuscript. All authors read and approved the final manuscript.

Funding

This study has been partially supported by DGAPA-UNAM under Project IN107720 and, under project UAL2020-RNM-B1980, by the *Consejería de Economía, Conocimiento, Empresas y Universidad* of Junta de Andalucía (Spain) and the EU 2014–2020 operative program of the European Regional Development Fund.

Availability of data and materials

The datasets generated during the current study are available from the corresponding author on reasonable request.

Declarations

Competing interests

The authors declare that they have no competing interests.

Author details

[1]Instituto de Ingeniería, Universidad Nacional Autónoma de México, Mexico, Mexico. [2]Departamento de Química y Física, Universidad de Almería, Almería, Spain. [3]Departamento de Ingeniería Civil, Universidad Eafit, Medellín, Colombia.

Received: 8 October 2022 Accepted: 27 January 2023
Published online: 27 February 2023

References

Aki K (1957) Space and time spectra of stationary stochastic waves, with special reference to microtremors. Bull Earthquake Res Inst 35:415–457
Aki K, Richards PG (2002) Quantitative Seismology. University Science Books, Sausalito
Alsop LE (1968) An orthonormality relation for elastic body waves. Bull Seismol Soc Am 58:1949–1954
Baena-Rivera M, Perton M, Sánchez-Sesma FJ (2016) Surface waves retrieval from Generalized Diffuse Fields in 2D synthetic models of alluvial valleys. Bull Seismol Soc Am 106:2811–2816
Bouchon M (2003) A review of the discrete wavenumber method. Pure Appl Geoph 160:445–465

Bouchon M, Aki K (1977) Discrete wave number representation of seismic source wave fields. Bull Seismol Soc Am 67:259–277
Campillo M, Paul A (2003) Long-range correlations in the diffuse seismic coda. Science 299:547–549
Chao C-C (1960) Dynamical response of an elastic half-space to tangential surface loadings. J Appl Mech 27(3):559–567
Feng X, Zhang H (2018) Exact closed-form solutions for Lamb's problem. Geophys J Int 214:444–459
Hennino R, Trégourès N, Shapiro NM, Margerin L, Campillo M, van Tiggelen B, Weaver RL (2001) Observation of equipartition of seismic waves in Mexico. Phys Rev Lett 86:3447–3450
Herrera I (1964) On a method to obtain a Green's function for a multi-layered half space. Bull Seismol Soc Am 54:1087–1096
Johnson LR (1974) Green's function for Lamb's problem. Geophys J Int 37:99–131
Kausel E (2006) Fundamental solutions in elastodynamics: a compendium. Cambridge University Press, Cambridge
Kausel E (2013) Lamb's problem at its simplest. Proc R Soc A. https://doi.org/10.1098/rspa.2012.0462
Lamb H (1904) On the propagation of tremors over the surface of an elastic solid. Phil Trans R Soc A 203:1–42
Lapwood ER (1949) The disturbance due to a line source in a semi-infinite elastic medium. Phil Trans R Soc A 242:63–100
Liu T, Feng X, Zhang H (2016) On Rayleigh wave in half-space: an asymptotic approach to study the Rayleigh function and its relation to the Rayleigh wave. Geophys J Int 206:1179–1193
Margerin L (2009) Generalized eigenfunctions of layered elastic media and application to diffuse fields. J Acoust Soc Am 125(1):164–174
Margerin L, Campillo M, van Tiggelen BA, Hennino R (2009) Energy partition of seismic coda waves in layered media: theory and application to pinyon flats observatory. Geophys J Int 177(2):571–585
Miller GF, Pursey H (1954) The field and radiation impedance of mechanical radiators on the free surface of a semi-infinite isotropic solid. Proc R Soc A 223:521–541
Miller GF, Pursey H (1955) On the partition of energy between elastic waves in a semi-infinite solid. Proc R Soc A 233:55–69
Mooney HM (1974) Some numerical solutions for Lamb's problem. Bull Seismol Soc Am 64:473–491
Paul A, Campillo M, Margerin L, Larose E, Derode A (2005) Empirical synthesis of time-asymmetrical Green function from the correlation of coda waves. J Geophys Res. https://doi.org/10.1029/2004JB003521
Pekeris CL (1955) The seismic surface pulse. Proc Natl Acad Sci USA 41:469–480
Pérez-Ruiz JA, Luzón F, Sánchez-Sesma FJ (2008) Retrieval of elastic Green's tensor near a cylindrical inhomogeneity from vector correlations. Commun Comput Phys 3(1):250–270. https://doi.org/10.1029/2006GL026454
Perton M, Sánchez-Sesma FJ (2016) Green's function calculation from equipartition theorem. J Acoust Soc Am 140:1309–1318
Perton M, Sánchez-Sesma FJ, Rodríguez-Castellanos A, Campillo M, Weaver RL (2009) Two perspectives on equipartition in diffuse elastic fields in three dimensions. J Acoust Soc Am 126:1125–1130
Piña-Flores J, Cárdenas-Soto M, García-Jerez A, Campillo M, Sánchez-Sesma FJ (2021) The search of diffusive properties in ambient seismic noise. Bull Seism Soc Am 111:1650–1660
Richards PG (1979) Elementary solutions to Lamb's problem for a point source and their relevance to three-dimensional studies of spontaneous crack propagation. Bull Seismol Soc Am 69:947–956
Sánchez-Sesma FJ, Campillo M (2006) Retrieval of the Green's function from cross correlation: the canonical elastic problem. Bull Seismol Soc Am 96:1182–1191
Sánchez-Sesma FJ, Pérez-Ruiz JA, Campillo M, Luzón F (2006) Elastodynamic 2D Green function retrieval from cross-correlation: canonical inclusion problem. Geophys Res Lett 33(L13305):1–6
Sánchez-Sesma FJ, Pérez-Ruiz JA, Luzón F, Campillo M, Rodríguez-Castellanos A (2008) Diffuse fields in dynamic elasticity. Wave Motion 45:641–654
Sánchez-Sesma FJ, Weaver RL, Kawase H, Matsushima S, Luzón F, Campillo M (2011) Energy partitions among elastic waves for dynamic surface loads in a semi-infinite solid. Bull Seismol Soc Am 101:1704–1709
Sánchez-Sesma FJ, Iturrarán-Viveros U, Perton M (2016) Some properties of Green's functions for diffuse field interpretation. Math Methods in the Appl Sci. https://doi.org/10.1002/mma3947
Stokes GG (1849) On the dynamic theory of diffraction. Trans Cambridge Phil Soc 9:1–62
van Manen D-J, Robertsson JO, Curtis A (2005) Modeling of wave propagation in inhomogeneous media. Phys Rev Lett 94(16):164301
van Manen D-J, Curtis A, Robertsson JO (2006) Interferometric modelling of wave propagation in inhomogeneous elastic media using time-reversal and reciprocity. Geophysics 71:S147–S160. https://doi.org/10.1190/1.221321
Wapenaar K (2004) Retrieving the elastodynamic Green's function of an arbitrary inhomogeneous medium by cross correlation. Phys Rev Lett. https://doi.org/10.1103/PhysRevLett.93.254301
Weaver RL (1982) On diffuse waves in solid media. J Acoust Soc Am 71:1608–1609
Weaver RL (1984) Diffuse waves in finite plates. J Sound Vib 94:319–335
Weaver RL (1985) Diffuse elastic waves at a free surface. J Acoust Soc Am 78:131–136
Weaver RL (2010) Equipartition and retrieval of Green's function. Earthq Sci 23:1–6
Weaver RL, Lobkis OI (2001) Ultrasonics without a source: Thermal fluctuation correlations at MHz frequencies. Phys Rev Lett 87(134301):1–4

Publisher's Note